ACS Catalysis

pubs.acs.org/acscatalysis Research Article

Reactant-Induced Dynamic Stabilization of Highly Dispersed Pt Catalysts on Ceria Dictating the Reactivity of CO Oxidation

Chen Chen, Jia-Lan Chen, Li Feng, Jianyu Hu, Xuting Chai, Jin-Xun Liu,* and Wei-Xue Li*

Cite This: ACS Catal. 2024, 14, 3504−3513 Read Online

ACCESS | Metrics & More | Article Recommendations | Supporting Information

ABSTRACT: The reactant-induced dynamics of catalysts under harsh conditions have a profound impact on their reactivity and stability, and identification of the underlying principle and active sites is vital for the rational design of catalysts. Based on a comprehensive first-principles investigation, we reveal here a reactant-induced dynamic stabilization of the highly dispersed Pt complexes that formed on ceria surfaces and their decisive role in CO oxidation. Compared to those of Pt nanoparticles, reactant-stabilized single-nuclear $Pt_1(CO)_m$ and/or multinuclear $Pt_8(CO)_n$ complexes prevail under CO-rich conditions on the defective CeO_2 (111), (110), and (100) surfaces considered. At lower temperatures, the $Pt_1(CO)$ complexes emerge as active sites for CO oxidation, whereas at higher temperatures, the active sites transit dynamically to the $Pt_8(CO)_9$ complexes. We found that oxygen defects not only stabilize the complexes but also promote activity via the facile Mars−van Krevelen mechanism. These insights reveal the great impact of the reactant-interference structure−activity relationship under operando conditions.

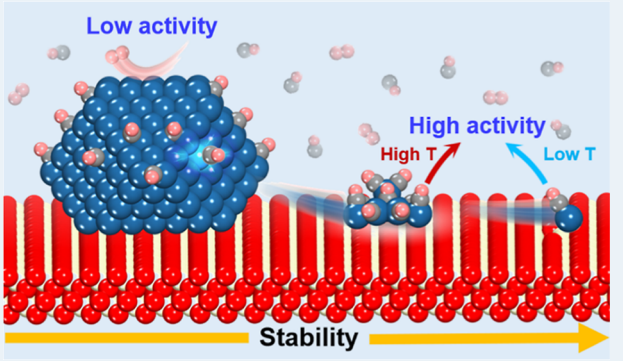

KEYWORDS: *catalyst-induced dynamics by reactants, platinum complexes, theoretical modeling, platinum on cerium oxide, CO oxidation, reaction mechanisms*

INTRODUCTION

Heterogeneous catalysis drives a myriad of industrial processes, from energy production to environmental protection, and its success relies critically on the ability to transform raw materials into valuable products with high activity, selectivity, and stability. The activity and selectivity of catalysts are essentially determined by their composition and structure for the desired bond-breaking and making involved.[1] Under elevated temperatures and pressures, the presence of reactants significantly changes the chemical state and structure of the catalyst during catalytic reactions.[2] For supported metal nanocatalysts, the reactants can accelerate sintering and/or disintegrate into small metal complexes, eventually deactivating the catalysts.[3] However, for fully exposed clusters and/or single-atom catalysts, reactants can fully populate highly coordinately unsaturated metal atoms with increased flexibility and distinct functionalities.[4−6] Revealing the structural dynamics and impact on activity and stability among supported single atoms, clusters, and nanoparticle catalysts under operational conditions is of paramount importance for the rational design of catalysts.[7]

Ceria-supported platinum (Pt/CeO_2) is widely employed as a preeminent catalyst for mitigating exhaust gas emissions due to the exceptional oxygen storage capacities inherent in CeO_2 supports. For Pt/CeO_2-catalyzed CO oxidation, fully exposed Pt clusters and single-atom catalysts (denoted as Pt_C/CeO_2 and Pt_1/CeO_2, respectively) were synthesized to maximize the atomic utilization efficiency of Pt.[8−11] However, the evolution of the stability and structural dynamics of Pt_C/CeO_2, Pt_1/CeO_2, and nanoparticles (Pt_{NP}/CeO_2) under operating conditions and their impacts on CO oxidation remain the subject of ongoing debate. Depending on the conditions, the dispersion or agglomeration of Pt varies in the form of single atoms and/or clusters, and the catalytic activities change accordingly.[5,12] It was reported that atomically dispersed square Pt_1 exhibits low activity and/or acts as a spectator during CO oxidation,[13] while others have demonstrated that highly dispersed Pt_1 sites are very active for CO oxidation.[14] On the other hand, the as-prepared Pt_1 species was reported to be regenerated in situ as a highly active Pt_C during CO oxidation.[15] The formation of highly active sites at the Pt−CeO_2 interface was attributed to the high activity of Pt_C/CeO_2.[9,16,17] Nevertheless, the lack of uniformity in preparing

Received: November 18, 2023
Revised: January 23, 2024
Accepted: February 9, 2024

https://doi.org/10.1021/acscatal.3c05590
ACS Catal. 2024, 14, 3504−3513

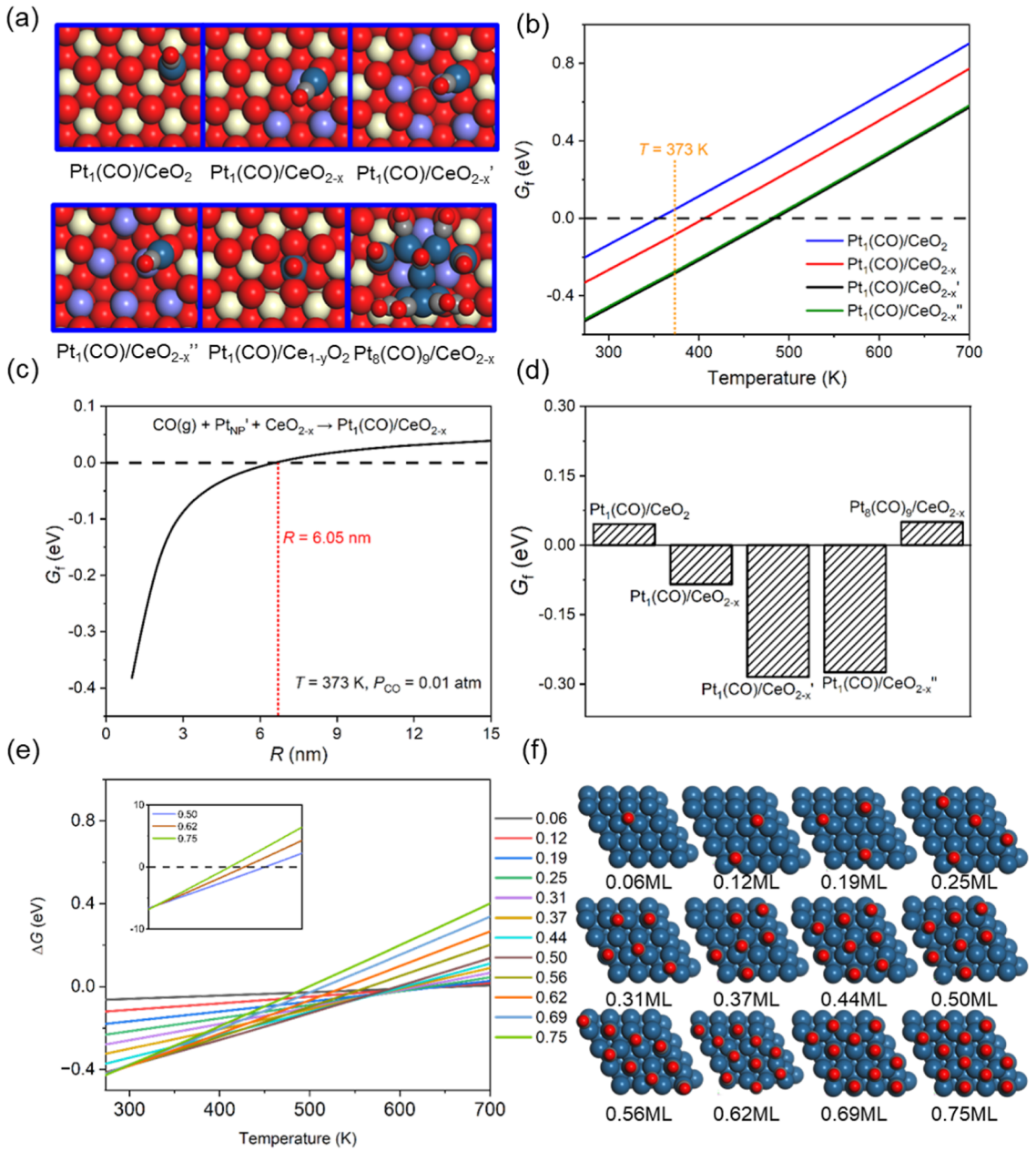

Figure 1. Structural analysis and stability assessment of the Pt/CeO_2 catalyst. (a) GCMC-DFT simulations yield optimized structures for single-nuclear $Pt_1(CO)$, $Pt_1/Ce_{1-y}O_2$, and multinuclear $Pt_8(CO)_9/CeO_{2-x}$ structures. (b) Temperature-dependent Gibbs formation energy ΔG of single-nuclear $Pt_1(CO)$ as a function of temperature at P_{CO} = 0.01 atm. (c) Gibbs formation energy variation of single-nuclear $Pt_1(CO)$ with Pt nanoparticle radius at T = 373 K and P_{CO} = 0.01 atm. (d) Stability comparisons between single-nuclear $Pt_1(CO)$ and multinuclear $Pt_8(CO)_9$ at T = 373 K and P_{CO} = 0.01 atm. (e,f) Phase diagram and CO-covered Pt(111) surface structures derived from KMC simulations.[15] Colors: Ce, Pt, O, and C atoms are represented by beige, blue, red, and gray spheres, respectively.

Pt/CeO_2 catalysts, often in a mixture of single atoms, clusters, and nanoparticles, which might change and transform dynamically depending on the reaction conditions, surface orientations, and defects,[17,18] prevents the identification of the true active species responsible for the observed activity. Investigating the functions of Pt_1, Pt_C, and Pt NP catalysts under operating conditions, their restructuring, and the authentic active centers for CO oxidation is a formidable task from both experimental and theoretical points of view.

Here, through a comprehensive first-principles-based multiscale investigation, we reveal the dynamic formation of active Pt_1 and Pt_C carbonyl complexes from Pt NPs under CO-rich conditions and their decisive role as active sites in catalyzing the oxidation of CO on various defective ceria surfaces. Ab initio thermodynamic calculations showed that the presence of CO tends to disintegrate small Pt NPs on defective $CeO_2(111)$ into Pt carbonyl complexes. Using basin-hopping-driven grand canonical Monte Carlo (GCMC) simulation, two disintegrated porotype complexes, namely, single-nuclear complexes ($Pt_1(CO)_{1,2}$) and cluster complexes (here as a showcase, $Pt_8(CO)_{8,9}$), were identified under CO-rich conditions,[19] and ab initio molecular dynamics (AIMD) further confirmed that these complexes transform dynamically at elevated temperatures. For CO oxidation, first-principles kinetics simulations revealed that the number of active sites changes from the $Pt_1(CO)$ complexes to the $Pt_8(CO)_9$ complexes with

https://doi.org/10.1021/acscatal.3c05590
ACS Catal. 2024, 14, 3504−3513

increasing temperature. Here, oxygen defects play a central role not only by stabilizing Pt carbonyl complexes but also by increasing activity via the facile Mars van Krevelen (MvK) mechanism. To investigate the influence of redox properties and the local coordination of oxide supports, stepped CeO_2 (111), (110), and (100) surfaces were considered. These findings highlight the impact of reactants on the dynamic formation of highly active single-atom and cluster catalysts, dictating catalytic reactivity under reaction conditions.

RESULTS AND DISCUSSION

Structures of the Pt/CeO_2 Catalyst under a CO Atmosphere. To establish a structure−function relationship, it is necessary to determine the stability of the structure under realistic operational conditions. Here, we reveal the chemical stability of Pt/CeO_2 catalysts across single atoms, clusters, and NPs in the presence of CO, revealing the strong interplay between metals, reactants, and supports during CO oxidation. Two prototype Pt_1 species were studied, namely, Pt_1 adsorbed on the surface and trapped in the Ce lattice vacancy, noted as $Pt_1/Ce_{1-y}O_2$.[8,20] A representative yet computationally fordable magic-numbered Pt_8 cluster[21] on CeO_2(111) was used to simulate a Pt_C/CeO_2 catalyst. GCMC simulations were used to determine the composition and structure of the Pt_1/CeO_2 and Pt_C/CeO_2 catalysts under typical CO-rich conditions (T = 373 K, P_{CO} = 0.01 atm), corresponding to the CO oxidation reaction.[17] For comparison, the low-index Pt(111), (110), and (100) surfaces were employed to present the large Pt_{NP} catalyst on support, given their maximized surface area—an assertion supported by surface energy calculations and the Wulff construction method,[22] and corresponding CO coverage was identified through kinetic Monte Carlo (KMC) simulations[23] and GCMC simulations.

Compared to that of bare Pt_1 on CeO_2(111), the formation of Pt_1(CO) carbonyl complexes can be thermodynamically exothermic due to the strong interaction between Pt and CO, although the adsorption of another CO to form dicarbonyls becomes endothermic (Figures 1a,c and S1−S3). Namely, in the presence of CO, Pt_1 alone cannot exist but can exist in the form of the Pt_1(CO) complex on CeO_2(111). In fact, its free energy is even lower than the chemical potential of supported 3 nm bare Pt NPs, as determined by the Gibbs−Thomson equation (Figure S2) below 350 K and with P_{CO} = 0.01 atm. This implies that the corresponding Pt NPs are unstable and tend to disintegrate from CO. The presence of CO can reduce the ceria surface area and generate additional oxygen vacancies, as determined by our thermodynamic calculations (Figures S4 and S5), in agreement with the experimental results.[11,24] In turn, the oxygen vacancies (V_O) further stabilize the Pt_1(CO) complexes, and the CO-induced disintegration of the Pt NPs can be maintained at an even higher temperature of 400 K (Figure 1b). These results indicate that neither the supported Pt NPs nor the bare Pt_1 are stable on CeO_{2-x}(111); instead, the Pt_1(CO) complexes are thermodynamically more favorable under typical CO conditions (T < 400 K and P_{CO} = 0.01 atm). Note that Pt_1 could be trapped at the Ce^{4+} vacancies, and it is very stable and free from agglomeration due to its strong exothermic formation energy of −3.91 eV with respect to the Pt bulk metal (Figure S6). Generally, the Ce vacancy (V_{Ce}) is more difficult to generate than the V_O.[25] Like the Pt/TiO_2 system,[26] while Ce vacancies (V_{Ce}) can form under oxygen treatment, enabling Pt to be trapped within these vacancies.[15] However, the formation of Ce vacancies under low-temperature CO oxidation conditions is difficult, leading to a minimal occurrence of the $Pt_1/Ce_{1-y}O_2$(111) structure, as illustrated in Figure S7.

Utilizing GCMC simulations with varying numbers of CO molecules, the most favorable structure of the Pt_8 cluster on CeO_{2-x}(111) at 373 K and P_{CO} = 0.01 atm, specifically the $Pt_8(CO)_9$ carbonyl complexes, was identified (Figure 1a). Any further alteration in the number of CO molecules would increase the free energy, and the adsorption of eight CO molecules on the Pt_8 cluster is less stable than that on $Pt_8(CO)_9$. Our calculations align with prior experimental findings that demonstrate full coverage of CO on Pt clusters during CO oxidation.[17] These complexes are energetically nearly the same as the chemical potential of supported 3 nm Pt NPs (Figure 1d) but become more favorable at a higher CO chemical potential (Figure S5). Interestingly, $Pt_8(CO)_9$ exhibited a Gibbs free formation energy close to that of Pt_1(CO), with a difference of less than 0.15 eV under various CO atmospheres (Figures 1 and S5), indicating that these two complexes might coexist and change dynamically on CeO_{2-x}(111). To investigate this phenomenon, we employed constrained AIMD simulations along with an umbrella-enhanced sampling method. Intriguingly, these two entities exhibit facile transformation at 373 K (Figure 2; Videos S1 and S2). In fact, the calculated Gibbs free energy surface shows that the corresponding forward and backward transformation barriers are 1.23 and 1.38 eV, respectively (Figure 2),

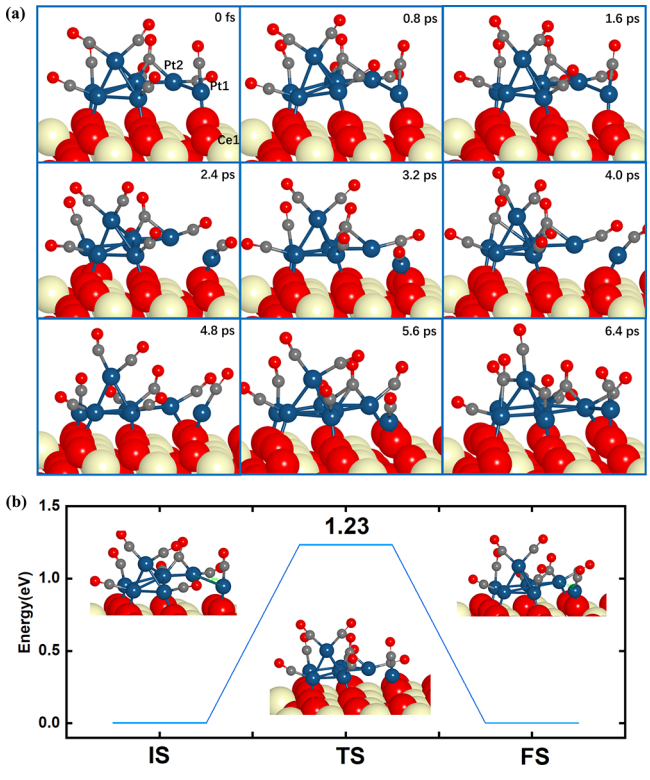

Figure 2. Identification of the dynamic structural evolution between $Pt_8(CO)_9/CeO_{2-x}$(111) and $Pt_1(CO)/CeO_{2-x}$(111). (a) Constrained AIMD simulations unveil the dynamic structural evolution between $Pt_8(CO)_9/CeO_{2-x}$(111) and $Pt_1(CO)/CeO_{2-x}$(111). Representative snapshot structures from AIMD simulations conducted at T = 373 K are depicted. (b) PES diagram illustrates the dynamic structural evolution between $Pt_8(CO)_9/CeO_{2-x}$(111) and $Pt_1(CO)/CeO_{2-x}$ at T = 373 K.

https://doi.org/10.1021/acscatal.3c05590
ACS Catal. 2024, 14, 3504−3513

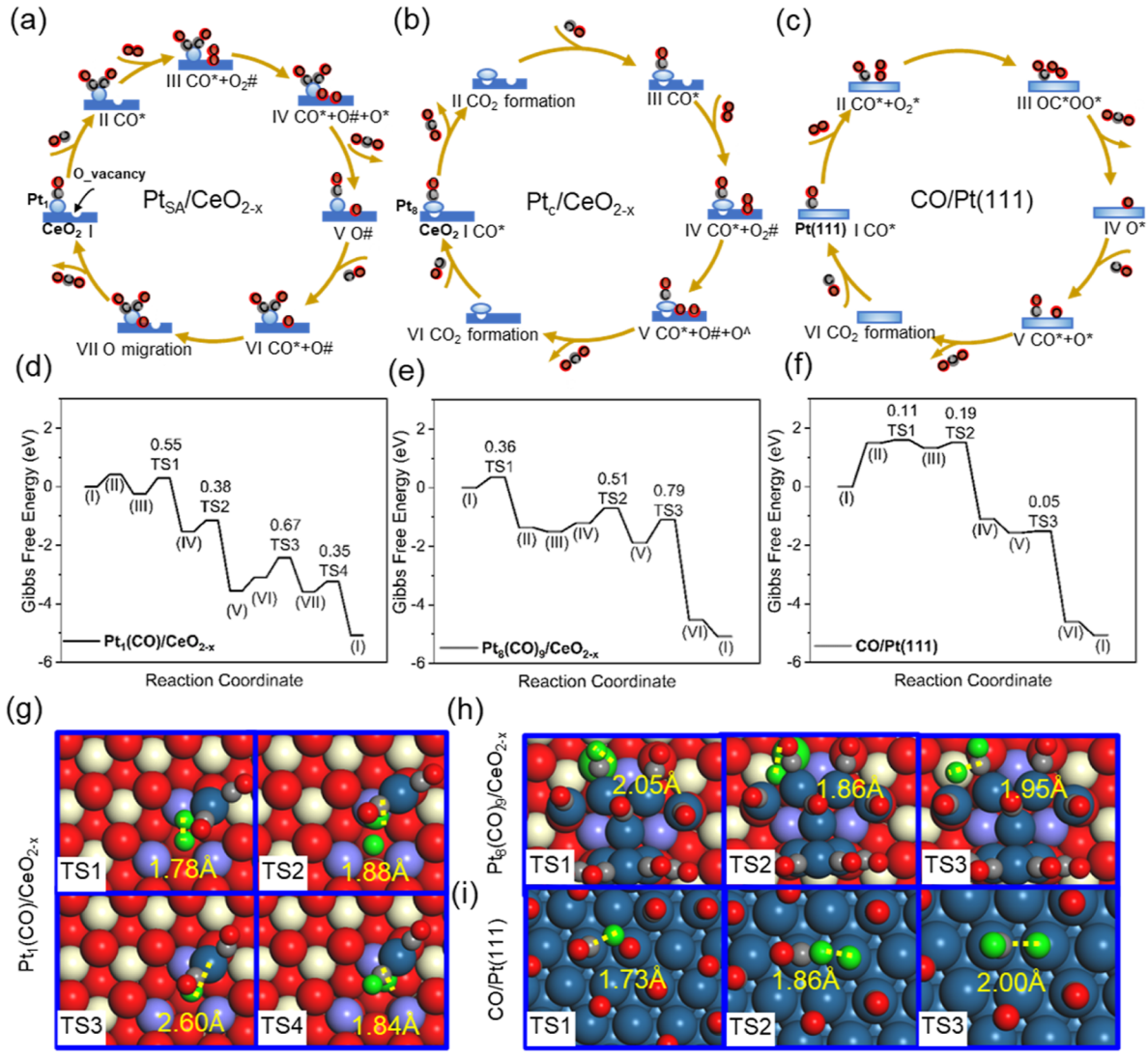

Figure 3. CO oxidation mechanism study across various Pt/CeO_2 catalyst structures. (a–c) Schemes for CO oxidation cycles over the Pt_1/CeO_{2-x}, Pt_C/CeO_{2-x}, and CO/Pt(111) structures. * and # represent the Pt sites and oxygen vacancies on the CeO_2 support, respectively. (d–f) Gibbs free energy diagrams for CO oxidation. The elementary activation barriers are indicated in eV. (g–i) Geometric structures of key transition states involved in CO oxidation over different types of Pt/CeO_2 catalysts. The distances between the two reacting fragments at the transition state are indicated in Å. The green spheres are O atoms involved in CO oxidation.

underscoring the dynamic changes between $Pt_8(CO)_9$ and $Pt_1(CO)$ under elevated temperatures. This complicates the identification of the active sites and reaction mechanisms, but it has not been addressed before.

Compared to the $Pt_8(CO)_9$ and $Pt_1(CO)$ complexes on supports, Pt NPs remain stable when their size is larger than ~6 nm (Figure 1c); moreover, the low-index Pt(111), (110), and (100) surfaces are used as representative models for extended Pt nanoparticle catalysts. To identify the corresponding structure and coverage under reaction conditions, we employed KMC simulations[23] to explore CO adsorption on Pt(111) at different coverages (Figure 1e,f). Through atomistic thermodynamic analysis, we found that under the specified conditions of T = 373 K and P_{CO} = 0.01 atm, the saturation coverage of CO is 0.50 ML (half at the top sites and half at the bridge sites), herein termed CO/Pt(111), which is used in the following control investigation. GCMC simulations were further carried out to ascertain the surface coverage of CO on the Pt(110) and Pt(100) surfaces under reaction conditions (T = 373 K and P_{CO} = 0.01 bar). These simulations revealed that the CO surface coverage is 11/16 ML for Pt(100) and 15/16 ML for Pt(110).

CO Oxidation Mechanism. To identify the active sites and catalytic role of $Pt_1/Ce_{1-y}O_2(111)$, $Pt_1(CO)$, and $Pt_8(CO)_9$ supported on $CeO_{2-x}(111)$, and CO/Pt(111) considered thus far, we calculated the potential energy surfaces (PESs) for CO oxidation. For $Pt_1(CO)/CeO_{2-x}(111)$ and $Pt_1/Ce_{1-y}O_2(111)$, the optimized PESs follow the MvK mechanism, in agreement with the literature.[11,27] CO starts by adsorbing on the Pt_1 sites, initiating a reaction with lattice oxygen to produce CO_2. Subsequently, the O_2 dissociates, regenerating lattice oxygen to complete the reaction cycle. Notably, the reaction of CO with lattice oxygen on $Pt_1(CO)/CeO_{2-x}(111)$ is highly endothermic by 1.45 eV, making CO oxidation unfavorable at low temperatures. However, there is an alternative scenario in which the strongly preadsorbed CO molecule can be considered a spectator in the reaction, and another CO molecule adsorbs to participate in the actual

https://doi.org/10.1021/acscatal.3c05590
ACS Catal. 2024, 14, 3504–3513

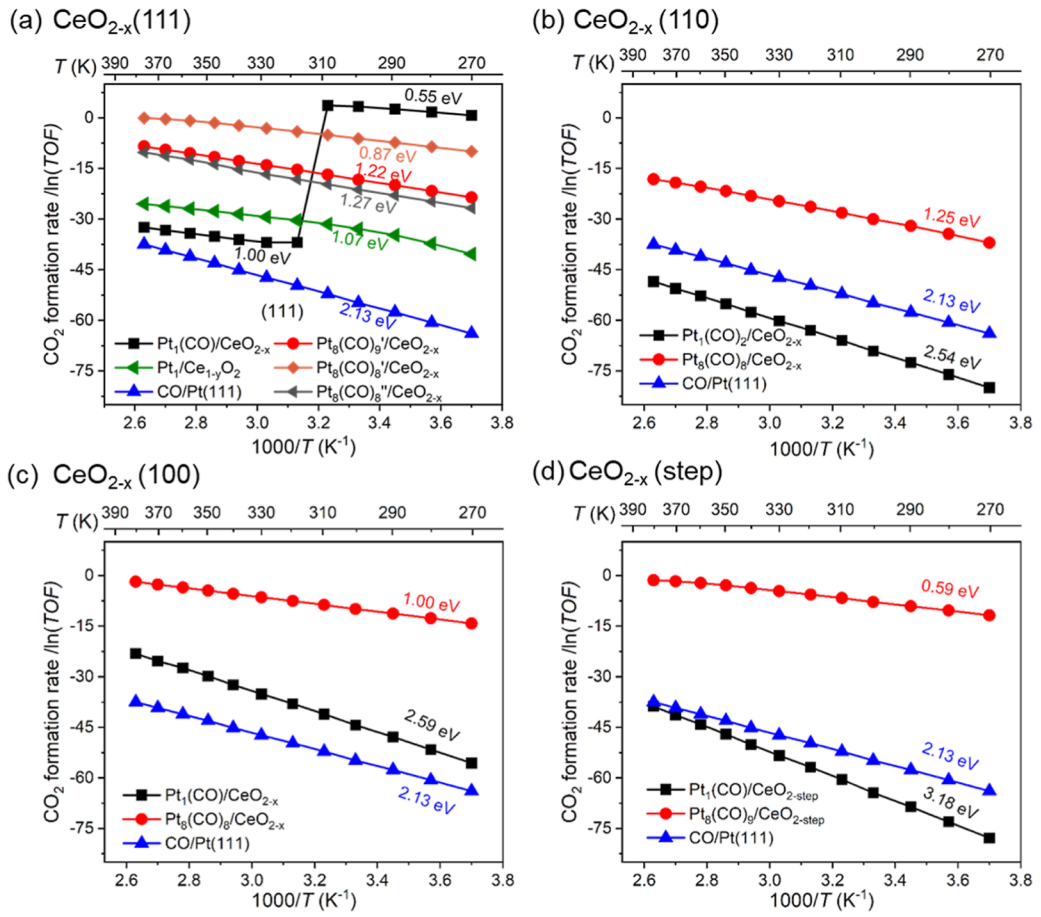

Figure 4. The turnover frequency (TOF, s^{-1}) of CO oxidation is computed by microkinetic simulations. The computed TOF of CO oxidation over the CeO_{2-x}(111) (a), (110) (b), (100) (c), and stepped (111) (d) surfaces supported $Pt_1(CO)_m$ (m = 1−2) and $Pt_8(CO)_n$ (n = 8 and 9), as well as CO/Pt(111) surfaces. The CO oxidation rates of the metastable $Pt_8(CO)_9$, metastable $Pt_8(CO)_8'$, and $Pt_8(CO)_8''$ over the CeO_{2-x}(111) surface are calculated. The apparent activation barriers (in eV) indicated are predicted using the Arrhenius equation.

reaction. In this case, when an incoming CO molecule adsorbs at a single Pt atom, it can react with lattice oxygen in a thermodynamically exothermic manner, resulting in a more energetically favorable process (Figures 3a and S10). As a result, $Pt_1(CO)/CeO_{2-x}$(111) is highly active for CO oxidation, following an MvK with elementary reaction barriers consistently lower than 0.67 eV (Figure 3d). The migration of lattice oxygen to the neighboring Pt site emerges as the step with the highest elementary barrier of 0.67 eV (Figures 3d,g, and S10), potentially acting as the rate-determining step (RDS) governing the activity. Notably, $Pt_1(CO)$ complexes on oxygen vacancy-rich surfaces can lead to a reduction in activity, as evidenced by an increase in the barrier of at least 0.15 eV associated with oxygen migration (Figures S10−S12). For $Pt_1/Ce_{1-y}O_2$ (111), the optimized PES is plotted in Figure S13, where a high barrier of 1.57 eV for O_2 dissociation alone limits its overall activity, particularly compared to $Pt_1(CO)/CeO_{2-x}$(111).

For $Pt_8(CO)_9/CeO_{2-x}$(111), a new reaction pathway emerges, where CO reacts with oxygen atoms from O_2 dissociation to form CO_2 at the perimeter sites between $Pt_8(CO)_9$ and CeO_{2-x}(111) (Figure 3b), with no longer migration of the lattice oxygen. In fact, O_2 dissociation could occur either on the CeO_{2-x}(111) surface exclusively to heal the oxygen vacancies (Figure S14) or at the perimeter sites between $Pt_8(CO)_9$ and CeO_{2-x}(111) to heal one oxygen vacancy but retain another oxygen atom coordinating to the Pt atoms of the complexes (Figures 3e,h, and S15). For the former pathway, only one Pt atom is involved, but two atoms are involved in the latter pathway, although lattice oxygen is involved in both pathways. For $Pt_8(CO)_9/CeO_{2-x}$(111), the maximum elementary barriers for these two pathways are comparable at 0.79 and 0.86 eV, respectively, and are slightly higher than those of $Pt_1(CO)/CeO_{2-x}$(111) by at least 0.12 eV (Figure 3d,e). This indicates that $Pt_1(CO)$ might be more active than less-populated $Pt_8(CO)_9$, particularly at low temperatures. However, at elevated temperatures, $Pt_8(CO)_9$ might be more active than $Pt_1(CO)$ due to the relatively weak CO bonding on the latter (E_{CO} = −0.36 eV).

For comparison, we note that CO oxidation on CO/Pt(111) follows a well-established Langmuir−Hinshelwood mechanism[28] via the so-called peroxide-like OCOO intermediate. This mechanism is found to be energetically more favorable than the O_2 dissociation pathway by 0.36 eV (Figures 3c,f,i and, S16 and S17). Compared to $Pt_1(CO)$ and $Pt_8(CO)_9$ supported on CeO_{2-x}(111), the limiting barrier through the OCOO intermediate on the CO/Pt(111) bond is 0.19 eV lower. However, the highly endothermic adsorption of O_2 (ΔG_{O2} = 1.49, 0.87, and 1.58 eV) on the CO/Pt(111), CO/Pt(110), and CO/Pt(100) surfaces significantly suppresses its overall activity, as shown below.

https://doi.org/10.1021/acscatal.3c05590
ACS Catal. 2024, 14, 3504−3513

Microkinetic simulations[29] were used to quantitatively assess the intrinsic activity of the Pt/CeO_2 catalysts considered thus far (Tables S1−S4). Note that the CO/Pt(111), CO/Pt(110), and CO/Pt(100) surfaces exhibit the highest apparent activation barrier E_{app} (2.13−2.70 eV) for CO oxidation, resulting in the lowest oxidation rate over the whole range of temperatures considered (Figure 4a) due to CO poisoning, in agreement with the observed diminished activity on Pt NPs at relatively lower T.[30] The E_{app} of $Pt_1(CO)/CeO_{2-x}(111)$ is only 0.55 eV, which is notably lower than those of $Pt_8(CO)_9/CeO_{2-x}(111)$ (1.22 eV) and $Pt_1/Ce_{1-y}O_2(111)$ (1.07 eV) at T values less than 318 K (Figure 4a). Consequently, the $Pt_1(CO)/CeO_{2-x}(111)$ structure exhibits the highest reaction rate within the temperature range below 318 K. Compared to $Pt_1/Ce_{1-y}O_2$, although $Pt_8(CO)_9/CeO_{2-x}(111)$ has a higher E_{app}, it has a relatively higher rate because less CO* can adsorb at the Pt_1 site over the former surface during CO oxidation (Figure S28). We note that when T > 318 K, the activity of $Pt_1(CO)/CeO_{2-x}(111)$ decreases dramatically due to the strong tendency for desorption of another weakly bound CO (Figure S28). As a result, $Pt_8(CO)_9/CeO_{2-x}(111)$ became the most active catalyst. The $Pt_1/Ce_{1-y}O_2$ surface, often employed as a model for single-atom catalysts, consistently exhibits a lower reactivity than those of $Pt_1(CO)/CeO_{2-x}(111)$ and $Pt_8(CO)_9/CeO_{2-x}(111)$.

We further studied the CO oxidation mechanism over two metastable isomers, namely, $Pt_8(CO)_8'$ and $Pt_8(CO)_8''$, which are less stable than $Pt_8(CO)_9$ by 0.02 and 0.13 eV, respectively. This indicates that these metastable isomers can exist as the most stable isomers under CO oxidation conditions but are distinguished by the varying local environments surrounding the Pt atoms. The calculated structures, PES diagram, and microkinetic simulation results for CO oxidation over the metastable $Pt_8(CO)_8'$ and $Pt_8(CO)_8''$ isomers are shown in Figures 4a, S22, S30, S31, S37, and Table S3. Although both the most stable $Pt_8(CO)_9$ and metastable $Pt_8(CO)_8'$ exhibit similar high activation barriers for CO oxidation, the latter isomer demonstrates greater activity due to its stronger O_2 adsorption by 0.79 eV (Figure S30 and Table S3). We found the metastable $Pt_8(CO)_8'$ structure has a low E_{app} of 0.87 eV and exhibits the highest CO oxidation activity at 0.14 s^{-1}, surpassing the most stable $Pt_8(CO)_9/CeO_{2-x}(111)$ structure. However, the $Pt_8(CO)_8''$ isomer has the lowest CO oxidation activity due to its highest CO oxidation barrier of 1.27 eV (Figure S31 and Table S3). Although the activity of the metastable isomer $Pt_8(CO)_8'$ is greater than that of the most stable $Pt_8(CO)_9$, the predominant catalyst for CO oxidation at low temperatures is the Pt single atom, while at higher temperatures, the metastable Pt cluster takes precedence (Figures 4a and S22). Therefore, $Pt_1(CO)/CeO_{2-x}(111)$ emerges as the active site for CO oxidation in the low-T regime, while $Pt_8(CO)_9/CeO_{2-x}(111)$ takes precedence in CO oxidation in the high-T regime. Notably, variations in the choice of exchange−correlation functional, including the PBE, RPBE, and PBE + vdW functional, in DFT calculations only induced a marginal change in barriers (less than 0.12 eV, Table S6 and Figure S18) and did not change the trend found above.

Surface Structure Sensitivity of the CeO_2 Support. Stepped and open CeO_{2-x} surfaces, which expose lower coordinated surface Ce^{3+}/Ce^{4+} and/or O atoms, may interact distinctively with Pt and influence the results above (Figures S23−S31). Accordingly, we investigated the polar and reconstructed $CeO_2(100)$ surface, where half of the oxygen atoms on the top surface were eliminated. Moreover, we considered the stepped $CeO_2(111)$ surface, which was represented by a $p(4 \times 4)$ $CeO_2(111)$ surface model with two columns of topmost O−Ce−O layers removed. Although previous investigations have highlighted the formation of carbonate on ceria support and its substantial impact on support reconstruction,[31] this topic is beyond the focus of this specific study. On oxygen-defective $CeO_2(110)$, (100), and stepped (111) surfaces, GCMC simulations reveal that Pt_8 clusters can stably adsorb eight or nine CO molecules at 373 K and P_{CO} = 0.01 atm, denoted as $Pt_8(CO)_8/CeO_{2-x}(110)$, $Pt_8(CO)_8/CeO_{2-x}(100)$, and $Pt_8(CO)_9/CeO_{2\text{-step}}$ (Figure S21), respectively, indicating little influence of the support on the formation of large Pt_C carbonyl complexes. However, these surfaces considerably stabilize the Pt_1 carbonyl complexes. In fact, the stabilizations of $Pt_1(CO)$ on $CeO_{2-x}(110)$ and (100) and $Pt_1(CO)_2$ on the $CeO_{2\text{-step}}$ are so strong that they even enable the disintegration of the infinitely large bulk Pt (Figure S20).

Note that, compared to those on the Pt_C complexes, the Pt_1 complexes on these surfaces are energetically more favorable. On $CeO_{2-x}(110)$, the difference in energy was small (less than 0.19 eV) (Figure S20), indicating that both complexes could coexist on these surfaces, as was the case for $CeO_{2-x}(111)$. However, on the $CeO_{2-x}(100)$ and $CeO_{2\text{-step}}$ surfaces, the formation of the $Pt_1(CO)$ and $Pt_1(CO)_2$ complexes is highly exothermic and energetically much more favorable than that of the Pt_C complexes by at least 1.19 eV. In other words, on the $CeO_{2-x}(100)$ and $CeO_{2\text{-step}}$ surfaces, the Pt_1 carbonyl complexes will be the dominant sites. The calculated reaction rates for these three surfaces show that the Pt_8 carbonyl complexes are more active than the Pt_1 carbonyl complexes and Pt NPs at T, ranging from 270 to 380 K (Figure 4b−d). However, on $CeO_{2-x}(110)$, the activity of the $Pt_8(CO)_8$ complex is approximately 6 orders of magnitude lower than that of $CeO_{2-x}(111)$. On the $CeO_{2-x}(100)$ and CeO_2-steps, although the activity of the $Pt_8(CO)_8$ complexes is higher than that of $CeO_{2-x}(111)$, their low concentration limits their contribution to the overall activity. Beyond the $CeO_{2-x}(111)$ surface, the clusters consistently exhibit higher activity than single atoms on the $CeO_{2-x}(110)$, (100), and stepped (111) surfaces. Accounting for metastable Pt isomers might widen the activity gap between these forms and cannot alter the conclusion that Pt clusters are more active than single-atom catalysts over $CeO_{2-x}(110)$, (100), and stepped (111) surfaces.

Our theoretical modeling validates recent research in experiments and reveals dynamic transformations, migrations, and redistributions among single atoms, clusters, and nanoparticles, particularly during CO oxidation over the Pt/CeO_2 catalyst,[15,32] which offers a comprehensive scenario for rationalizing the experiments required for further investigation. Specifically, Pt clusters exhibit higher CO oxidation activity than Pt_1 at elevated temperatures due to the presence of reactive interfacial oxygen species.[9,16,17] Moreover, the high activity observed for CO oxidation in the Pt_1/CeO_2 catalyst[14] can be attributed to Pt (CO), whereas the low activity observed for CO oxidation[13] may be linked to $Pt_1/Ce_{1-y}O_2$.

Degree-of-rate-control (DRC) analysis[33] was employed to elucidate the disparities in activity for CO oxidation across the Pt_1 and Pt_C carbonyl complexes and Pt NPs over the various surfaces considered. The greater the value of the DRC is for a particular step, the more significant is the impact of its rate

https://doi.org/10.1021/acscatal.3c05590
ACS Catal. 2024, 14, 3504−3513

constant on the overall reaction rate. A positive value indicates that increasing the rate constant will lead to an increase in the net reaction; such steps are referred to as RDS. Our investigation unveils several potential RDSs for CO oxidation, including oxygen migration from CeO_2 to a single Pt site, removal of oxygen species from Pt sites, and O_2 adsorption/dissociation, and these results are particularly evident for the $Pt_1(CO)_{1/2}$ and $Pt_8(CO)_{8/9}$ catalysts (Figures S25 and S26). This exploration further established a correlation between reactivity, quantified by the TOF, and the binding strength of surface lattice oxygen species across different Pt/CeO_2 structures with variations in the CeO_{2-x} surfaces (illustrated in Figure 5). The enhanced lattice oxygen binding strength on

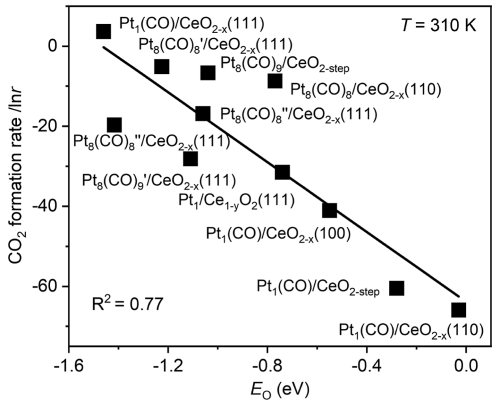

Figure 5. Linear scaling relationship identifications and dynamic transitions in activity among single atoms, clusters, and nanocatalysts. Linear scaling relationships between CO_2 formation rates (ln r) and O adsorption energies across various structures, including single-nuclear $Pt_1(CO)/CeO_{2-x}$, multinuclear $Pt_8(CO)_n/CeO_{2-x}$ (n = 8 or 9), and $Pt_1/Ce_{1-y}O_2(111)$ structures.

the CeO_{2-x} support corresponds to a heightened CO oxidation TOF, suggesting that the binding energy of surface lattice oxygen serves as an indicator of oxidation activity on Pt/CeO_2 catalysts. Therefore, strategies aimed at augmenting oxidation performance over Pt/CeO_2 catalysts may involve manipulating the binding strength of the surface lattice oxygen.

CONCLUSIONS

In summary, our comprehensive theoretical investigations have illuminated the reactant-mediated transitions in the structure and composition of Pt/CeO_2 catalysts under the reaction conditions, shedding light on CO oxidation. The CO-stabilized Pt_1 atom, instead of the Pt single atom alone, on the defective $CeO_2(111)$ surface, was identified as the active site for CO oxidation at low temperature and was much more active than the Pt-doped $CeO_2(111)$ ($Pt_1/Ce_{1-y}O_2$) catalyst. At higher temperatures, CO-stabilized multinuclear $Pt_8(CO)_9$ clusters dominate the process of driving CO oxidation. The presence of oxygen defects not only reinforces the stability of these single-molecule and multinuclear complexes but also significantly amplifies their activity via the facile MvK mechanism. The clusters exhibit greater activity than single atoms on the (110), (100), and stepped (111) ceria supports. This work not only offers a promising theoretical blueprint for deciphering reactant-induced highly dispersed catalysts under reaction conditions but also extends its relevance to diverse catalytic systems involving CO as reactants, intermediates, or products.

COMPUTATIONAL METHODS

Spin-polarized DFT calculations were performed using the Vienna Ab initio Simulation Package code (VASP).[34] The projector augmented wave potentials[35] and revised Perdew–Burke–Ernzerhof (RPBE) functional[36] were used to describe the electron–ion and exchange–correlation interactions. The DFT + U approach[37] was adopted to describe strongly correlated cerium 4f states in partially reduced ceria. In our DFT calculations utilizing the RPBE, PBE, and PBE + vdW functionals, we set the U value specifically at 5 eV.[38] The plane-wave cutoff energy was set to 300 eV for the genetic algorithm (GA), GCMC, and AIMD simulations. Geometry optimization was used to converge when the forces on each atom were less than 0.10 eV/Å to accelerate the GA-driven GCMC simulations.

A $p(4 \times 4)$ slab including two O–Ce–O atomic layers was used to model the $CeO_2(111)$, (110), (100), and (111) step surfaces, where the top O–Ce–O atomic layers in the supercell, the adsorbed Pt species and adsorbates, were fully relaxed for all the DFT calculations. This choice was based on findings that extending the $CeO_2(111)$ slab model to encompass three O–Ce–O layers resulted in negligible changes—less than 0.2 eV—in oxygen vacancy formation energy, Pt_1 adsorption energy and CO adsorption energy on Pt_1/CeO_2 and the formation energy of Pt_8 supported on $CeO_{2-x}(111)$. We depicted the polarized $CeO_2(100)$ surface as a reconstructed form of $CeO_2(100)$ by eliminating half of its surface oxygen atoms, a structure that has been validated by STM characterization.[39] Brillouin zone sampling was restricted to the Γ point. A $p(4 \times 4)$ slab with three metal layers was used to model the Pt(111) surface, where the top Pt atom layer and adsorbates were allowed to relax. The Brillouin zone was sampled with a 4 × 4 × 1 Monkhorst–Pack[40] K-point grid for the $p(4 \times 4)$ Pt(111) surface. The neighboring slabs were separated by a vacuum of more than 10 Å. The cutoff energy and force convergence criteria were specified as 400 and 0.05 eV/Å, respectively, for the CO oxidation mechanism studies. The transition states involved in CO oxidation were located by the climbing-image nudged elastic band method[41] with a force tolerance of 0.05 eV/Å. The vibrational frequencies and corresponding modes were calculated to verify the identified transition states.

The electronic energy of the O_2 molecule was calculated by placing the O_2 gas molecules in a vacuum box with lattice constants of a = 10 Å, b = 11 Å, and c = 12 Å using the tetrahedron method with Blöchl corrections.[42] The presence of a CO atmosphere has a significant influence on the stability of the Pt_1/CeO_2 catalyst, which can be quantified by the standard Gibbs formation energy relative to Pt nanoparticles as follows

$$G_f = E_{Pt_1/CeO_2} - G_{nCO} - E_{CeO_2} - E_{NP}' \quad (1)$$

Where E_{Pt1/CeO_2}, E_{CeO_2}, E_{NP}', and G_{nCO} are the energies of the CO-ligand-decorated Pt single atom over the CeO_2 support, the CeO_2 surface, a metal atom in Pt nanoparticles, and the Gibbs free energy of gaseous CO, respectively. The total energy of a Pt nanoparticle was calculated by the Gibbs–Thomson equation[43]

$$E_{NP} = E_{bulk} + \frac{3\Omega\gamma}{R} \quad (2)$$

where E_{bulk}, Ω, γ, and R are the DFT-calculated energy of a particle in the bulk phase, the molar volume of a Pt metal

https://doi.org/10.1021/acscatal.3c05590
ACS Catal. 2024, 14, 3504–3513

atom, the overall surface energy of the metal particle, and the radius of the nanoparticle, respectively. The adopted values of Ω and γ are 9.09 cm^3/mol and 1.59 J/m^2, respectively.[44]

AIMD simulations were performed to reveal the dynamic structural evolution of $Pt_8(CO)_9/CeO_{2-x}$ and $Pt_1(CO)/CeO_{2-x}$ under a CO atmosphere by using the LASP code.[45] The Nose−Hoover thermostat[46] was used for *NVT* ensemble sampling at three temperatures—273, 323, and 373 K—for 3 ps AIMD simulations. Umbrella sampling methods were employed to accelerate this process and accurately calculate the energy barriers for structural transformations. The MD time step was set to 1 fs.

■ ASSOCIATED CONTENT

Supporting Information

The Supporting Information is available free of charge at https://pubs.acs.org/doi/10.1021/acscatal.3c05590.

(MP4)

(MP4)

Detailed methodology, DFT calculation structures, potential energy surface, phase diagram, microkinetic simulation results, and calculated energetics (DOCX)

■ AUTHOR INFORMATION

Corresponding Authors

Jin-Xun Liu − *Key Laboratory of Precision and Intelligent Chemistry, Department of Chemical Physics, iChem, University of Science and Technology of China, Hefei, Anhui 230026, China; Hefei National Laboratory, University of Science and Technology of China, Hefei 230088, China;* orcid.org/0000-0002-7499-4197; Email: jxliu86@ustc.edu.cn

Wei-Xue Li − *Key Laboratory of Precision and Intelligent Chemistry, Department of Chemical Physics, iChem, University of Science and Technology of China, Hefei, Anhui 230026, China; Hefei National Laboratory, University of Science and Technology of China, Hefei 230088, China;* orcid.org/0000-0002-5043-3088; Email: wxli70@ustc.edu.cn

Authors

Chen Chen − *Key Laboratory of Precision and Intelligent Chemistry, Department of Chemical Physics, iChem, University of Science and Technology of China, Hefei, Anhui 230026, China*

Jia-Lan Chen − *Key Laboratory of Precision and Intelligent Chemistry, Department of Chemical Physics, iChem, University of Science and Technology of China, Hefei, Anhui 230026, China*

Li Feng − *Key Laboratory of Precision and Intelligent Chemistry, Department of Chemical Physics, iChem, University of Science and Technology of China, Hefei, Anhui 230026, China*

Jianyu Hu − *Hefei National Research Center for Physical Science at the Microscale, University of Science and Technology of China, Hefei, Anhui 230026, China*

Xuting Chai − *Key Laboratory of Precision and Intelligent Chemistry, Department of Chemical Physics, iChem, University of Science and Technology of China, Hefei, Anhui 230026, China*

Complete contact information is available at: https://pubs.acs.org/10.1021/acscatal.3c05590

Author Contributions

C.C. and J.-L.C. contributed equally to this work. J.X.L. and W.X.L. conceived the idea and supervised and directed the project. C.C., C.J.L., F.L., and J.H. performed the theoretical calculations and analyzed the DFT data. All the authors discussed the results and wrote and commented on the paper.

Notes

The authors declare no competing financial interest.

■ ACKNOWLEDGMENTS

This work was supported by the Key Technologies R&D Program of China (2021YFA1502804), the Strategic Priority Research Program of the Chinese Academy of Science (XDB0450102), the National Natural Science Foundation of China (22172150, 22221003, and 22222306), the National Natural Science Foundation of Anhui Province (2108085QB62), the USTC Research Funds of the Double First-Class Initiative (YD2060002012), K. C. Wong Education (GJTD-2020-15), the Innovation Program for Quantum Science and Technology (2021ZD0303302), the Fundamental Research Funds for the Central Universities (20720220009) and high-performance computational resources provided by the University of Science and Technology of China, and the Hefei Advanced Computing Center. We thank Samuel D. Young at the University of Michigan for reading the paper.

■ REFERENCES

(1) (a) Therrien, A. J.; Hensley, A. J. R.; Marcinkowski, M. D.; Zhang, R.; Lucci, F. R.; Coughlin, B.; Schilling, A. C.; McEwen, J.-S.; Sykes, E. C. H. An atomic-scale view of single-site Pt catalysis for low-temperature CO oxidation. *Nat. Catal.* **2018**, *1* (3), 192−198. (b) van Deelen, T. W.; Hernández Mejía, C.; de Jong, K. P. Control of metal-support interactions in heterogeneous catalysts to enhance activity and selectivity. *Nat. Catal.* **2019**, *2* (11), 955−970.

(2) (a) Poths, P.; Alexandrova, A. N. Theoretical perspective on operando spectroscopy of fluxional nanocatalysts. *J. Phys. Chem. Lett.* **2022**, *13* (19), 4321−4334. (b) Shi, X.; Lin, X.; Luo, R.; Wu, S.; Li, L.; Zhao, Z. J.; Gong, J. Dynamics of heterogeneous catalytic processes at operando conditions. *JACS Au* **2021**, *1* (12), 2100−2120.

(3) Liu, L. C.; Meira, D. M.; Arenal, R.; Concepcion, P.; Puga, A. V.; Corma, A. Determination of the evolution of heterogeneous single metal atoms and nanoclusters under reaction conditions: which are the working catalytic sites? *ACS Catal.* **2019**, *9* (12), 10626−10639.

(4) Liu, L. C.; Corma, A. Evolution of isolated atoms and clusters in catalysis. *Trends Chem.* **2020**, *2* (4), 383−400.

(5) Jones, J.; Xiong, H.; DeLaRiva, A. T.; Peterson, E. J.; Pham, H.; Challa, S. R.; Qi, G.; Oh, S.; Wiebenga, M. H.; Pereira Hernández, X. I.; et al. Thermally stable single-atom platinum-on-ceria catalysts via atom trapping. *Science* **2016**, *353* (6295), 150−154.

(6) (a) Lu, Y.; Wang, J.; Yu, L.; Kovarik, L.; Zhang, X.; Hoffman, A. S.; Gallo, A.; Bare, S. R.; Sokaras, D.; Kroll, T.; et al. Identification of the active complex for CO oxidation over single-atom Ir-on-$MgAl_2O_4$ catalysts. *Nat. Catal.* **2019**, *2* (2), 149−156. (b) Jeong, H.; Kwon, O.; Kim, B.-S.; Bae, J.; Shin, S.; Kim, H.-E.; Kim, J.; Lee, H. Highly durable metal ensemble catalysts with full dispersion for automotive applications beyond single-atom catalysts. *Nat. Catal.* **2020**, *3* (4), 368−375. (c) Gu, J.; Jian, M.; Huang, L.; Sun, Z.; Li, A.; Pan, Y.; Yang, J.; Wen, W.; Zhou, W.; Lin, Y.; et al. Synergizing metal-support interactions and spatial confinement boosts dynamics of atomic nickel for hydrogenations. *Nat. Nanotechnol.* **2021**, *16* (10), 1141−1149.

(7) Mou, T. Y.; Pillai, H. S.; Wang, S. W.; Wan, M. Y.; Han, X.; Schweitzer, N. M.; Che, F. L.; Xin, H. L. Bridging the complexity gap in computational heterogeneous catalysis with machine learning. *Nat. Catal.* **2023**, *6* (2), 122−136.

(8) Wang, H.; Liu, J.-X.; Allard, L. F.; Lee, S.; Liu, J.; Li, H.; Wang, J.; Wang, J.; Oh, S. H.; Li, W.; et al. Surpassing the single-atom

catalytic activity limit through paired Pt-O-Pt ensemble built from isolated Pt1 atoms. *Nat. Commun.* **2019**, *10* (1), 3808.
(9) Lu, Y.; Zhou, S.; Kuo, C.-T.; Kunwar, D.; Thompson, C.; Hoffman, A. S.; Boubnov, A.; Lin, S.; Datye, A. K.; Guo, H.; et al. Unraveling the intermediate reaction complexes and critical role of support-derived oxygen atoms in CO oxidation on single-atom Pt/CeO_2. *ACS Catal.* **2021**, *11* (14), 8701−8715.
(10) Muravev, V.; Spezzati, G.; Su, Y.-Q.; Parastaev, A.; Chiang, F.-K.; Longo, A.; Escudero, C.; Kosinov, N.; Hensen, E. J. Interface dynamics of Pd-CeO_2 single-atom catalysts during CO oxidation. *Nat. Catal.* **2021**, *4* (6), 469−478.
(11) Jiang, D.; Yao, Y.; Li, T.; Wan, G.; Pereira-Hernandez, X. I.; Lu, Y.; Tian, J.; Khivantsev, K.; Engelhard, M. H.; Sun, C.; et al. Tailoring the local environment of platinum in single-atom Pt_1/CeO_2 catalysts for robust low-temperature CO oxidation. *Angew. Chem., Int. Ed. Engl.* **2021**, *60* (50), 26054−26062.
(12) (a) Daelman, N.; Capdevila-Cortada, M.; López, N. Dynamic charge and oxidation state of Pt/CeO_2 single-atom catalysts. *Nat. Mater.* **2019**, *18* (11), 1215−1221. (b) Pereira-Hernández, X. I.; DeLaRiva, A.; Muravev, V.; Kunwar, D.; Xiong, H.; Sudduth, B.; Engelhard, M.; Kovarik, L.; Hensen, E. J.; Wang, Y.; et al. Tuning Pt-CeO_2 interactions by high-temperature vapor-phase synthesis for improved reducibility of lattice oxygen. *Nat. Commun.* **2019**, *10* (1), 1358.
(13) (a) Ke, J.; Zhu, W.; Jiang, Y.; Si, R.; Wang, Y.-J.; Li, S.-C.; Jin, C.; Liu, H.; Song, W.-G.; Yan, C.-H.; et al. Strong local coordination structure effects on subnanometer PtO_x clusters over CeO_2 nanowires probed by low-temperature CO oxidation. *ACS Catal.* **2015**, *5* (9), 5164−5173. (b) Ding, K.; Gulec, A.; Johnson, A. M.; Schweitzer, N. M.; Stucky, G. D.; Marks, L. D.; Stair, P. C. Identification of active sites in CO oxidation and water-gas shift over supported Pt catalysts. *Science* **2015**, *350* (6257), 189−192.
(14) Chen, J.; Wanyan, Y.; Zeng, J.; Fang, H.; Li, Z.; Dong, Y.; Qin, R.; Wu, C.; Liu, D.; Wang, M.; et al. Surface engineering protocol to obtain an atomically dispersed Pt/CeO_2 catalyst with high activity and stability for CO oxidation. *ACS Sustain. Chem. Eng.* **2018**, *6* (11), 14054−14062.
(15) Zhang, Z.; Tian, J.; Lu, Y.; Yang, S.; Jiang, D.; Huang, W.; Li, Y.; Hong, J.; Hoffman, A. S.; Bare, S. R.; et al. Memory-dictated dynamics of single-atom Pt on CeO_2 for CO oxidation. *Nat. Commun.* **2023**, *14* (1), 2664.
(16) (a) Gänzler, A. M.; Casapu, M.; Vernoux, P.; Loridant, S.; Cadete Santos Aires, F. J.; Epicier, T.; Betz, B.; Hoyer, R.; Grunwaldt, J. D. Tuning the structure of platinum particles on ceria in situ for enhancing the catalytic performance of exhaust gas catalysts. *Angew. Chem., Int. Ed.* **2017**, *56* (42), 13078−13082. (b) Kim, Y.; Oh, D. G.; Cho, S. J.; Khivantsev, K.; Kwak, J. H. Catalytic behavior of Pt single-atoms supported on CeO_2. *Catal. Today* **2024**, *425*, 114298.
(17) Lu, Y.; Thompson, C.; Kunwar, D.; Datye, A. K.; Karim, A. M. Origin of the high CO oxidation activity on CeO_2 supported Pt nanoparticles: weaker binding of CO or facile oxygen transfer from the support? *ChemCatChem* **2020**, *12* (6), 1726−1733.
(18) (a) Kopelent, R.; van Bokhoven, J. A.; Szlachetko, J.; Edebeli, J.; Paun, C.; Nachtegaal, M.; Safonova, O. V. Catalytically active and spectator Ce^{3+} in ceria-supported metal catalysts. *Angew. Chem.* **2015**, *127* (30), 8852−8855. (b) Gänzler, A. M.; Casapu, M.; Maurer, F.; Störmer, H.; Gerthsen, D.; Ferre, G.; Vernoux, P.; Bornmann, B.; Frahm, R.; Murzin, V.; et al. Tuning the Pt/CeO_2 interface by in situ variation of the Pt particle size. *ACS Catal.* **2018**, *8* (6), 4800−4811. (c) Trovarelli, A.; Llorca, J. Ceria catalysts at nanoscale: how do crystal shapes shape catalysis? *ACS Catal.* **2017**, *7* (7), 4716−4735. (d) Moncada, J.; Chen, X.; Deng, K.; Wang, Y.; Xu, W.; Marinkovic, N.; Zhou, G.; Martínez-Arias, A.; Rodriguez, J. A. Structural and chemical evolution of an inverse CeO_x/Cu catalyst under CO_2 hydrogenation: tunning oxide morphology to improve activity and selectivity. *ACS Catal.* **2023**, *13* (23), 15248−15258.
(19) (a) Zhang, Y.; Liu, J. X.; Qian, K.; Jia, A.; Li, D.; Shi, L.; Hu, J.; Zhu, J.; Huang, W. Structure sensitivity of Au-TiO_2 strong metal-support interactions. *Angew. Chem., Int. Ed.* **2021**, *60* (21), 12074−12081. (b) Pozdnyakova, O.; Teschner, D.; Wootsch, A.; Krohnert, J.; Steinhauer, B.; Sauer, H.; Toth, L.; Jentoft, F. C.; Knop-Gericke, A.; Paal, Z. Preferential CO oxidation in hydrogen (PROX) on ceria-supported catalysts, part I: oxidation state and surface species on Pt/CeO_2 under reaction conditions. *J. Catal.* **2006**, *237* (1), 1−16.
(20) Hatanaka, M.; Takahashi, N.; Tanabe, T.; Nagai, Y.; Dohmae, K.; Aoki, Y.; Yoshida, T.; Shinjoh, H. Ideal Pt loading for a Pt/CeO_2-based catalyst stabilized by a Pt-O-Ce bond. *Appl. Catal., B* **2010**, *99* (1−2), 336−342.
(21) Knight, W.; Clemenger, K.; de Heer, W. A.; Saunders, W. A.; Chou, M.; Cohen, M. L. Electronic shell structure and abundances of sodium clusters. *Phys. Rev. Lett.* **1984**, *52* (24), 2141−2143.
(22) Wulff, G. XXV. Zur Frage der Geschwindigkeit des Wachsthums und der Auflösung der Krystallflächen. *Z. Kristallogr. Cryst. Mater.* **1901**, *34* (1−6), 449−530.
(23) Shan, B.; Zhao, Y.; Hyun, J.; Kapur, N.; Nicholas, J. B.; Cho, K. Coverage-dependent CO adsorption energy from first-principles calculations. *J. Phys. Chem. C* **2009**, *113* (15), 6088−6092.
(24) Lee, J.; Ryou, Y.; Chan, X.; Kim, T. J.; Kim, D. H. How Pt interacts with CeO_2 under the reducing and oxidizing environments at elevated temperature: the origin of improved thermal stability of Pt/CeO_2 compared to CeO_2. *J. Phys. Chem. C* **2016**, *120* (45), 25870−25879.
(25) Zhang, C.; Michaelides, A.; King, D. A.; Jenkins, S. J. Anchoring sites for initial Au nucleation on CeO_2{111}: O vacancy versus Ce vacancy. *J. Phys. Chem. C* **2009**, *113* (16), 6411−6417.
(26) Thang, H. V.; Pacchioni, G.; DeRita, L.; Christopher, P. Nature of stable single atom Pt catalysts dispersed on anatase TiO_2. *J. Catal.* **2018**, *367*, 104−114.
(27) (a) Doornkamp, C.; Ponec, V. The universal character of the Mars and Van Krevelen mechanism. *J. Mol. Catal. A: Chem.* **2000**, *162* (1−2), 19−32. (b) Nie, L.; Mei, D.; Xiong, H.; Peng, B.; Ren, Z.; Hernandez, X. I. P.; DeLaRiva, A.; Wang, M.; Engelhard, M. H.; Kovarik, L.; et al. Activation of surface lattice oxygen in single-atom Pt/CeO_2 for low-temperature CO oxidation. *Science* **2017**, *358* (6369), 1419−1423.
(28) Alavi, A.; Hu, P.; Deutsch, T.; Silvestrelli, P. L.; Hutter, J. CO oxidation on Pt(111): an ab initio density functional theory study. *Phys. Rev. Lett.* **1998**, *80* (16), 3650−3653.
(29) Filot, I. A.; van Santen, R. A.; Hensen, E. J. The optimally performing Fischer−Tropsch catalyst. *Angew. Chem., Int. Ed.* **2014**, *126* (47), 12960−12964.
(30) Zaera, F.; Liu, J.; Xu, M. Isothermal study of the kinetics of carbon monoxide oxidation on Pt (111): rate dependence on surface coverages. *J. Chem. Phys.* **1997**, *106* (10), 4204−4215.
(31) (a) Li, C.; Sakata, Y.; Arai, T.; Domen, K.; Maruya, K.-i.; Onishi, T. Carbon monoxide and carbon dioxide adsorption on cerium oxide studied by Fourier-transform infrared spectroscopy. Part 1.—Formation of carbonate species on dehydroxylated CeO_2, at room temperature. *J. Chem. Soc., Faraday Trans. 1* **1989**, *85* (4), 929−943. (b) Chen, F.; Liu, D.; Zhang, J.; Hu, P.; Gong, X.-Q.; Lu, G. A DFT + U study of the lattice oxygen reactivity toward direct CO oxidation on the CeO_2(111) and (110) surfaces. *Phys. Chem. Chem. Phys.* **2012**, *14* (48), 16573−16580.
(32) Maurer, F.; Jelic, J.; Wang, J. J.; Ganzler, A.; Dolcet, P.; Woll, C.; Wang, Y. M.; Studt, F.; Casapu, M.; Grunwaldt, J. D. Tracking the formation, fate and consequence for catalytic activity of Pt single sites on CeO_2. *Nat. Catal.* **2020**, *3* (10), 824−833.
(33) (a) Campbell, C. T. Future directions and industrial perspectives micro-and macro-kinetics: their relationship in heterogeneous catalysis. *Top. Catal.* **1994**, *1* (3−4), 353−366. (b) Campbell, C. T. Finding the rate-determining step in a mechanism. *J. Catal.* **2001**, *204* (2), 520−524. (c) Stegelmann, C.; Andreasen, A.; Campbell, C. T. Degree of rate control: how much the energies of intermediates and transition states control rates. *J. Am. Chem. Soc.* **2009**, *131* (23), 8077−8082.
(34) (a) Kresse, G.; Furthmüller, J. Efficient iterative schemes for ab initio total-energy calculations using a plane-wave basis set. *Phys. Rev. B* **1996**, *54* (16), 11169−11186. (b) Kresse, G.; Furthmüller, J.

https://doi.org/10.1021/acscatal.3c05590
ACS Catal. 2024, 14, 3504−3513

Efficiency of ab-initio total energy calculations for metals and semiconductors using a plane-wave basis set. *Comput. Mater. Sci.* **1996**, *6* (1), 15−50.
(35) Kresse, G.; Joubert, D. From ultrasoft pseudopotentials to the projector augmented-wave method. *Phys. Rev. B* **1999**, *59* (3), 1758−1775.
(36) Hammer, B.; Hansen, L. B.; Nørskov, J. K. Improved adsorption energetics within density-functional theory using revised Perdew-Burke-Ernzerhof functionals. *Phys. Rev. B* **1999**, *59* (11), 7413−7421.
(37) (a) Anisimov, V. I.; Aryasetiawan, F.; Lichtenstein, A. First-principles calculations of the electronic structure and spectra of strongly correlated systems: the LDA + U method. *J. Phys.: Condens. Matter* **1997**, *9* (4), 767−808. (b) Dudarev, S. L.; Botton, G. A.; Savrasov, S. Y.; Humphreys, C.; Sutton, A. P. Electron-energy-loss spectra and the structural stability of nickel oxide: An LSDA + U study. *Phys. Rev. B* **1998**, *57* (3), 1505−1509.
(38) (a) Nolan, M.; Grigoleit, S.; Sayle, D. C.; Parker, S. C.; Watson, G. W. Density functional theory studies of the structure and electronic structure of pure and defective low index surfaces of ceria. *Surf. Sci.* **2005**, *576* (1−3), 217−229. (b) Nolan, M.; Parker, S. C.; Watson, G. W. The electronic structure of oxygen vacancy defects at the low index surfaces of ceria. *Surf. Sci.* **2005**, *595* (1−3), 223−232.
(39) Capdevila-Cortada, M.; López, N. Entropic contributions enhance polarity compensation for CeO_2(100) surfaces. *Nat. Mater.* **2017**, *16* (3), 328−334.
(40) Pack, J. D.; Monkhorst, H. J. Special points for Brillouin-zone integrations—a reply. *Phys. Rev. B* **1977**, *16* (4), 1748−1749.
(41) (a) Henkelman, G.; Uberuaga, B. P.; Jónsson, H. A climbing image nudged elastic band method for finding saddle points and minimum energy paths. *J. Chem. Phys.* **2000**, *113* (22), 9901−9904. (b) Henkelman, G.; Jónsson, H. Improved tangent estimate in the nudged elastic band method for finding minimum energy paths and saddle points. *J. Chem. Phys.* **2000**, *113* (22), 9978−9985.
(42) Blöchl, P. E.; Jepsen, O.; Andersen, O. K. Improved tetrahedron method for Brillouin-zone integrations. *Phys. Rev. B* **1994**, *49* (23), 16223−16233.
(43) (a) Ouyang, R.; Liu, J. X.; Li, W. X. Atomistic theory of Ostwald ripening and disintegration of supported metal particles under reaction conditions. *J. Am. Chem. Soc.* **2013**, *135* (5), 1760−1771. (b) Johnson, C. A. Generalization of the Gibbs-Thomson equation. *Surf. Sci.* **1965**, *3* (5), 429−444.
(44) (a) Lide, D. R. *CRC Handbook of Chemistry and Physics*; CRC Press, 2004. (b) Tran, R.; Xu, Z.; Radhakrishnan, B.; Winston, D.; Sun, W.; Persson, K. A.; Ong, S. P. Surface energies of elemental crystals. *Sci. Data* **2016**, *3* (1), 160080.
(45) Huang, S. D.; Shang, C.; Kang, P. L.; Zhang, X. J.; Liu, Z. P. LASP: fast global potential energy surface exploration. *Wiley Interdiscip. Rev. Comput. Mol. Sci.* **2019**, *9*, No. e1415.
(46) (a) Nosé, S. A unified formulation of the constant temperature molecular dynamics methods. *J. Chem. Phys.* **1984**, *81* (1), 511−519. (b) Hoover, W. G. Canonical dynamics: equilibrium phase-space distributions. *Phys. Rev. A* **1985**, *31* (3), 1695−1697.

https://doi.org/10.1021/acscatal.3c05590
ACS Catal. 2024, 14, 3504−3513